

Critical quantum metrology robust against dissipation and non-adiabaticity

Jia-Hao Lü,^{1,*} Wen Ning,^{1,*} Fan Wu,^{1,*} Ri-Hua Zheng,¹ Ken Chen,¹
Xin Zhu,¹ Zhen-Biao Yang,^{1,2,†} Huai-Zhi Wu,^{1,‡} and Shi-Biao Zheng^{1,2,§}

¹*Fujian Key Laboratory of Quantum Information and Quantum Optics,
College of Physics and Information Engineering,
Fuzhou University, Fuzhou, Fujian 350108, China*
²*Hefei National Laboratory, Hefei 230088, China*

(Dated: December 23, 2025)

Critical systems near quantum phase transitions were predicted to be useful for improvement of metrological precision, thanks to their ultra-sensitive response to tiny variations of the control Hamiltonian. Despite the promising perspective, realization of criticality-enhanced quantum metrology is an experimentally challenging task, mainly owing to decoherence and critical slowing down associated with the corresponding quantum state preparation. We here circumvent these problems by making use of the critical behaviors in the Jaynes-Cummings model, to which the signal field is coupled. The information is encoded in the qubit's excitation number, which displays a divergent changing rate at the critical point, and is extremely robust against decoherence and non-adiabatic effects. We demonstrate such a metrological protocol in a superconducting circuit, where an Xmon qubit, interacting with a resonator, is used as a probe for estimating the amplitude of a microwave field. The measured quantum Fisher information exhibits a critical quantum enhancement, confirming the potential of this system for quantum metrology.

I. TEASER

Ultrahigh precision measurement of a signal field is demonstrated by coupling it to an on-chip critical spin-boson system.

II. INTRODUCTION

The capability of accurately measuring a weak signal is crucial for advancing modern science and technology, exemplified by the detection of gravitational waves [1], which not only provides a direct evidence for the validity of general relativity, but also lays the experimental foundation for gravitational-wave astronomy. Quantum metrology aims to exploit quantum sources to improve the precision of measurement of special physical quantities, including the amplitude of a magnetic or electric field, the frequency of an oscillator, and the magnitude of a force [2, 3]. In conventional quantum metrological protocols, the signal is encoded in a quantum superposition of two components with highly distinct quantum numbers for a single element [4–6], e.g., Fock states $|0\rangle$ and $|N\rangle$ of a bosonic mode, or in a highly entangled state for many qubits [7–10]. With such encoding protocols, the achievable sensitivity can exhibit a scaling surpassing the standard quantum limit in principle. However, the vulnerability of these nonclassical states restricts their metrological practicalities, as the gain from

the increase of the system size is quickly cancelled out by the environment-induced decoherence effects [11].

Quantum critical phenomena represent an alternative quantum resource for realizing quantum sensing. When a quantum system evolves near the critical point of a phase transition [12], its properties exhibit dramatic changes in response to a slight variation of the governing Hamiltonian. These phenomena are useful for realizing criticality-enhanced quantum sensors [13–40], which aim to exploit critical systems to amplify the effects of the signal fields. In conventional critical metrological protocols [13–32, 41], the physical quantity is encoded in one specific eigenstate of the control Hamiltonian that is adiabatically steered towards the critical point. Benefitting from the adiabatic nature, this approach bears an intrinsic robustness against noises. However, it is an experimental challenge to meet the adiabatic condition close to a quantum phase transition, owing to the critical slowing down. To make a quantum system adiabatically follow one specific eigenstate, the changing rate of the control parameter usually needs to be much lower than the corresponding energy gaps. At the phase transition, these gaps vanish, which indicate the probability of leaking to other eigenstates is non-negligible when the system is approaching the critical point within a limited time. This inherent state leakage challenges the practical usefulness of such protocols. Recent theoretical investigations show that the adiabatic condition can be removed with dynamical approaches [30, 38–40], where the parameter to be estimated is encoded in the time-evolving state under a time-independent Hamiltonian, to which the physical quantity of interest is coupled. However, such dynamical protocols also require extremely long evolution time [42], furthermore, their performances depend on precise timing.

We here propose and demonstrate a critical quantum

* These authors equally contributed to the work.

† zbyang@fzu.edu.cn

‡ huaizhi.wu@fzu.edu.cn

§ t96034@fzu.edu.cn

metrological protocol, where the process to bring the system towards the critical point is significantly speeded up, but without loss of the robustness associated with adiabatic evolution. The sensor is composed of a single qubit and a photonic mode interacting with each other, referred to as the Jaynes-Cummings model (JCM) [43]. The signal field, whose amplitude is to be probed, couples to the bosonic mode, producing a continuous drive. Below the critical point, the system has a unique dark state, in which the signal is encoded. The energy gaps between this dark state and the nearest bright states are continually narrowed when approaching the critical point, where the average excitation numbers for both the photonic mode and the qubit exhibit diverging changing rates. The qubit excitation number, which serves as a robust indicator for estimating the amplitude of the signal field, is insensitive to state leakage. We demonstrate this criticality-enhanced metrology with a circuit quantum electrodynamics (QED) system, where a superconducting qubit and a microwave resonator form the JCM. The experimental results unambiguously demonstrate the robustness of the critical quantum sensing protocol.

III. RESULTS

A. Model

The theoretical model under consideration involves a photonic mode resonantly interacting with a qubit and driven by a signal field, whose amplitude is to be estimated, as schematically shown in Fig. 1(a). In the interaction picture, the system dynamics is described by the driven JCM (setting $\hbar = 1$) [44]

$$H = \Omega[(a^\dagger |g\rangle \langle e| + a |e\rangle \langle g|) + \varepsilon(a^\dagger + a)/2], \quad (1)$$

where a^\dagger and a denote the photonic creation and annihilation operators, $|g\rangle$ and $|e\rangle$ are the ground and excited state of the qubit, Ω represents the qubit-boson interaction strength, and ε characterizes the rescaled amplitude of the signal field coupled to the photonic mode. When $\varepsilon < 1$, the system possesses discrete eigenenergies, given by

$$\begin{aligned} E_0 &= 0, \\ E_{n,\pm} &= \pm\sqrt{n}\Omega A^{3/4}, \end{aligned} \quad (2)$$

where $A = 1 - \varepsilon^2$, as depicted in Fig. 1(b). We note that the eigenenergies are derived in the framework rotating at the frequency of the signal field, and will refer to them as quasi-energies [44]. The corresponding eigenstates are

$$\begin{aligned} |\psi_0\rangle &= S(r)|0\rangle|\phi_0\rangle, \\ |\psi_{n,\pm}\rangle &= S(r)D(\alpha_{n,\pm})(|n-1\rangle|\phi_1\rangle \pm |n\rangle|\phi_0\rangle)/\sqrt{2}, \end{aligned} \quad (3)$$

where $|n\rangle$ denotes the n -photon state, and $S(r) = \exp[r(a^2 - a^{\dagger 2})/2]$ and $D(\alpha_{n,\pm}) = \exp[\alpha_{n,\pm}(a^\dagger - a)]$ are respectively the squeezing and displacement operators for

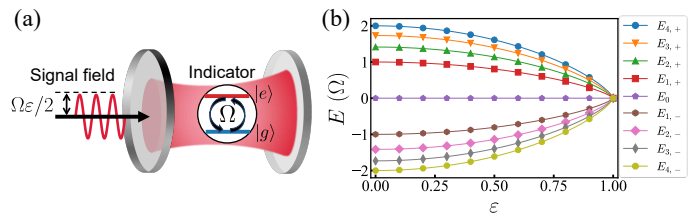


FIG. 1. (color online). Critical quantum sensing protocol. (a) Theoretical model. The model comprises a cavity mode interacting with the transition between the lower ($|g\rangle$) and upper state ($|e\rangle$) of a qubit, with the photonic swapping strength Ω . The signal field with an unknown rescaled amplitude ε is coupled to the resonator. (b) Quasi-energy spectrum. Such a model exhibits a highly nonlinear quasi-energy spectrum, with $E_0 = 0$ and $E_{n,\pm} = \pm\sqrt{n}\Omega(1 - \varepsilon^2)^{3/4}$. When $\varepsilon \ll 1$, the excitation number in the adiabatically evolved dark state is negligible, as a consequence of the photon blockade. At $\varepsilon = 1$ quasi-energy gaps vanish, leading to the breakdown of the photon blockade. Near this critical point, both the photon number and qubit excitation number exhibit a diverging changing rate in response to the variation of ε .

the photonic field, with $r = \frac{1}{4} \ln A$ and $\alpha_{n,\pm} = \mp\sqrt{n}\varepsilon$. $|\phi_{0,1}\rangle$ denote the qubit parts, given by

$$\begin{aligned} |\phi_0\rangle &= c_+ |g\rangle - c_- |e\rangle, \\ |\phi_1\rangle &= c_+ |e\rangle - c_- |g\rangle, \end{aligned} \quad (4)$$

with $c_{\pm} = (1 \pm \sqrt{A})^{1/2}/\sqrt{2}$. Hereafter, we will call $|\psi_0\rangle$ and $|\psi_{n,\pm}\rangle$ dark and bright eigenstates, respectively. The results show that when the driving strength is increased, the quasi-energy splittings are continually narrowed, all vanishing at the critical point $\varepsilon = 1$, beyond which the Hamiltonian H cannot be diagonalized so that the system does not possess a well-defined quasi-energy spectrum [45]. The quasi-energy level configuration can also be interpreted in terms of the competition between the JC coupling and the external driving. When the JC coupling dominates over the external driving, the system features the JC-like ladder, manifested by the \sqrt{n} -dependent splitting. If the external driving is dominant, the photonic mode is disentangled with the anharmonic qubit and the spectrum becomes a continuum. This spectral feature is associated with the dissipative-driven photon-blockade breakdown phase transition [46, 47]. We note these phase transitions cannot be described by the Ginzburg-Landau-Wilson symmetry-breaking paradigm, as the Hamiltonian itself does not possess the $U(1)$ symmetry of the JCM, which is explicitly broken by the drive.

We consider the system behaviors below but close to the critical point $\varepsilon = 1$. The associated average photon number, $\langle N \rangle_0 = \sinh^2 r$, displays a divergent behavior and thus can be used as a critical sensing indicator in principle. However, it is sensitive to leakage to the bright states $|\psi_{n,\pm}\rangle$, whose average photon number, $\langle N \rangle_n = 2n\varepsilon^2 e^{-2r} + n \cosh 2r - \frac{1}{2}$, is significantly distinct from that of the dark state. This sensitivity is unfavorable to improvement of the signal-to-noise ratio. In distinct

contrast, the qubit's excitation number is insensitive to leakage to the bright states, which can be caused either by decoherence or by the non-adiabatic effects. Due to this insensitivity, the qubit's excitation number can be used as a robust indicator for estimating the amplitude of the external drive. We note that the qubit responds to the change of the control field by interacting with the photonic mode, which is in a nonclassical state.

B. Numerical simulations

In our sensing protocol, the signal is encoded in the time-evolving eigenstate $|\psi_0\rangle$, which is separated from its nearest eigenstates by $E_{G,\min} = \Omega A^{3/4}$. The ratio between this energy gap and the ramping rate of the control parameter ε determines how well the system can be kept in the dark state. The lower this ramping rate, the smaller the leakage probability to the bright eigenstates. However, a longer evolution time would result in more serious decoherence effects. For a practical system, the attainable accuracy is limited by the non-adiabaticity and decoherence. As a compromise between these two effects, the dependence of ε on t is modeled as

$$\varepsilon = \sqrt{1 - (k^2 t^2 + 1)^{-1}}, \quad (5)$$

where k is the coefficient controlling the ramping velocity. Fig. 2(a) presents ε plotted as a function of t , where $k = 10$ MHz. To clearly show how well the system is restricted to the dark state during this quench process, we perform a simulation of the fidelity (F) as a function of ε , which is defined as $F = \langle \psi_0 | \rho | \psi_0 \rangle$, where ρ denotes the density operator for the system. ρ is calculated from the master equation, which includes the coherent dynamics governed by the Hamiltonian of Eq. (1), as well as the incoherent dissipations for both the qubit and the resonator (see Supplemental Material [48]). The numerical result is displayed in Fig. 2(b), where the qubit-resonator coupling strength and the energy dissipative rates are set to be the same as those in our experimental system. As expected, the fidelity drops fast when approaching the critical point, as a consequence of the leakage to bright states caused by decoherence and non-adiabatic effect.

As analyzed above, the average photon number is very sensitive to the state leakage. To provide quantitative evidence for this sensitivity, we simulate evolutions of the photon-number during quench process, defined as $\langle a^\dagger a \rangle = \text{Tr}(\rho a^\dagger a)$. The result is shown in Fig. 2(c), which confirms that even a slight leakage to the bright states can cause a significant deviation of the average photon number from that in the dark state. In contrast, the evolution of the qubit's $|e\rangle$ -state population (P_e) is robust against the state leakage, as shown in Fig. 2(d). As expected, when approaching the critical point, P_e calculated with different ramping velocities converge to that of the ideal dark eigenstate. This robustness is due to the fact that at the critical point, each of the bright states is a product state, where the qubit part is the same as

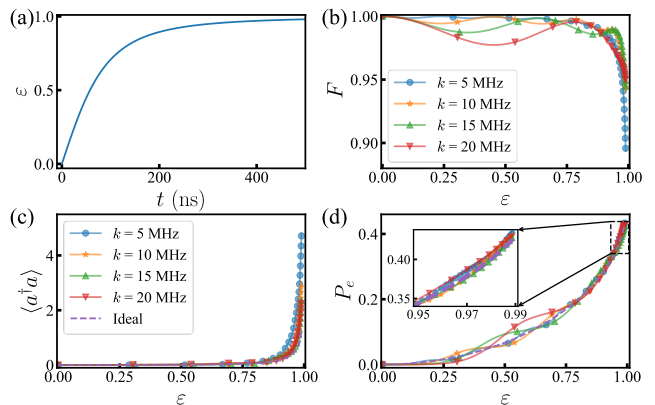


FIG. 2. (color online). Simulations of the quench process. (a) ε versus t . Here ε is varied according to Eq. (5) with $k = 10$ MHz. (b) Fidelities of the qubit-resonator state to the ideal dark state as functions of ε . In the simulation, the qubit-resonator coupling strength is set to $\Omega = 2\pi \times 20.9$ MHz, and the dissipation rates for the qubit and resonator are 0.05 MHz and 0.08 MHz, respectively. (c) Average photon number of the resonator and (d) qubit's excitation number versus ε for different k . The dashed lines in (c) and (d) denote the results for the ideal dark state. The nice agreement between the results from simulation and the ideal dark state demonstrates that the qubit's excited-state population is insensitive to the dissipations for both the qubit and the photonic mode.

in the dark state. Consequently, the evolution of P_e is robust against dissipation, non-adiabaticity, and imperfect timing. More importantly, near the critical point P_e almost displays the same dependence on ε for a quite wide range of k . This allows the problem associated with critical slowing down to be largely compensated by increasing k . For example, for the choice of $k = 10$ MHz, the ramping of ε from 0 to 0.99 is accomplished within a time $T \approx 700$ ns, which is much shorter than the energy relaxation times for the qubit and the photonic mode of the experimental system, $T_1^q = 20 \mu\text{s}$ and $T_1^p = 12 \mu\text{s}$. With this choice, the dependence of P_e on ε well coincides with that for the ideal dark state within the regime $0.8 < \varepsilon < 0.99$. For the ideal dark state, P_e becomes more sensitive to the change of ε when ε gets closer to 1, sharply increasing from 0.429 to 0.5 when ε is varied from 0.99 to 1, and exhibiting an infinite sensitivity at the critical point. However, for the real system, the sensitivity cannot be infinitely improved owing to decoherence and non-adiabatic effects, and consequently, a sharp increase of P_e to 0.5 at the critical point cannot be observed.

C. Experimental setup and results

The critical system is realized in a circuit QED architecture, which involves a bus resonator with a fixed frequency $\omega_r/2\pi \simeq 5.584$ GHz and five frequency-tunable Xmon qubits, one of which is used as the test qubit. The test qubit has an anharmonicity of $\chi \simeq 2\pi \times 0.245$ GHz.

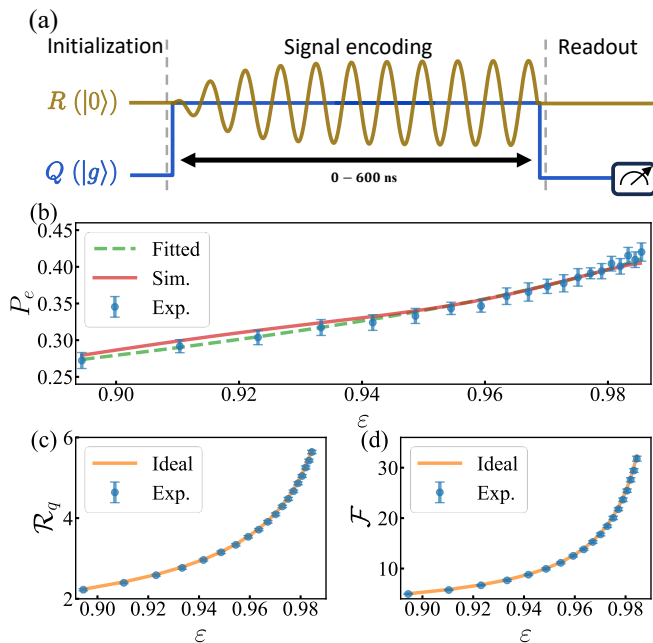


FIG. 3. (color online). Performance of the criticality-enhanced sensing. (a) Pulse sequence. The qubit (Q) is tuned from its idle frequency to the resonator's frequency. At the same time the signal field with a rescaled amplitude ϵ is coupled to the resonator. After the quench process, the qubit is biased back to its idle frequency for state readout. ϵ is the time-dependent function shown in Fig. 2(a). (b) Qubit's $|e\rangle$ -state population measured versus ϵ . The solid line denotes the simulation including the second-excited state of the Xmon, and the dashed line is the fitted function $P_e(\epsilon) = C(1 - \sqrt{A})/2$, with $C = 0.9899$. (c) Signal-to-noise ratio (\mathcal{R}_q) and (d) Fisher information (\mathcal{F}) versus ϵ . The values \mathcal{R}_q and \mathcal{F} depend both on P_e and on its derivative with respect to ϵ . The value of this derivative at each point is calculated with the fitted function $P_e(\epsilon)$. The solid lines in (c) and (d) denote the results for the ideal dark state.

The on-resonance photonic swapping rate between the qubit and the resonator is $\Omega \simeq 2\pi \times 20.9$ MHz. The energy decaying rates for the qubit and the resonator are $\kappa_q \simeq 0.05$ MHz and $\kappa_r \simeq 0.08$ MHz, respectively. The dephasing rate of the qubit, measured at its idle frequency is around 1.25 MHz. We note that the dephasing noises are highly suppressed by resonantly coupling to the photonic field, as a consequence of the dynamical decoupling [49].

Before the experiment, the resonator is in the vacuum and the test qubit is initially in its ground state at the idle frequency $\omega_0/2\pi = 5.35$ GHz, where it is effectively decoupled from the bus resonator since the corresponding detuning is much larger than Ω . The interaction between this qubit and the resonator is activated by tuning the qubit to the resonator's frequency. At the same time, the signal field with a rescaled amplitude ϵ is coupled to the resonator, continuously driving the photonic field. The experimental pulse sequence is shown in Fig. 3(a). The

rescaled field amplitude ϵ versus t is set to be the same as that shown in Fig. 2(a).

Due to the limited anharmonicity, the Xmon has a probability of leaking to levels higher than $|e\rangle$, which increases with the resonator's photon number. To suppress this leakage, we fine tune the detunings of the qubit and the resonator (see Supplemental Material). When ϵ reaches a preset value, the qubit is biased back to its idle frequency for state readout. The qubit's $|e\rangle$ -state populations, measured for different values of ϵ , are displayed in Fig. 3(b). The measured data well agree with the numerical simulation, where the Xmon's second-excited state $|f\rangle$ is included. The slight fluctuations are mainly caused by imperfect calibration of the amplitude of the signal field. In our experiment, ϵ is calibrated by coupling the signal field to the resonator for a given time, and then reading out the resonator's average photon number with an ancilla qubit (see Supplemental Material). The errors in this procedure make the calibrated value of ϵ deviate from the real value. The dashed line denotes the function $C(1 - \sqrt{A})/2$, fitted with the data measured within the range $0.9 < \epsilon < 0.985$, where the fitted parameter C is 0.9899, close to the ideal value $C = 1$. This agreement confirms that the critical behaviors of the qubit are well controlled.

The critical enhancement is manifested by the diverging changing rate of P_e in the dark state $|\psi_0\rangle$, given by $dP_e/d\epsilon = \epsilon/(2\sqrt{A})$, which tends to $1/[2\sqrt{2(1-\epsilon)}]$ when $1 - \epsilon \ll 1$. Consequently, in proximity of the critical point, a tiny variation of ϵ would result in dramatic responses of the qubit. The signal-to-noise ratio is given by

$$\mathcal{R}_q = \frac{dP_e/d\epsilon}{\Delta P_e}, \quad (6)$$

where $\Delta P_e = \sqrt{P_e(1-P_e)}$ denotes the standard deviation for measuring P_e (see Supplemental Material). In proximity of the critical point, \mathcal{R}_q is approximately given by $1/\sqrt{2(1-\epsilon)}$. \mathcal{R}_q versus ϵ [inferred from ϵ -dependence of P_e in Fig. 3(b)] is shown in Fig. 3(c). The performance of the quantum sensor can be further quantified by the Fisher information, defined as

$$\mathcal{F} = \frac{1}{P_e} \left(\frac{dP_e}{d\epsilon} \right)^2 + \frac{1}{P_g} \left(\frac{dP_g}{d\epsilon} \right)^2. \quad (7)$$

As shown in the Supplemental Material, \mathcal{F} is equal to the quantum Fisher information, thereby saturating the Cramér-Rao bound. Moreover, \mathcal{F} linearly scales with the square of the time, corresponding to the optimal Heisenberg scaling precision [27]. Fig. 3(d) presents the Fisher information evolution obtained from the measured P_e . Within the range $0.9 < \epsilon < 0.985$, the results for \mathcal{R}_q and \mathcal{F} both agree well with those calculated with the ideal dark state (solid lines).

The most remarkable feature of our scheme is the incorporation of the intrinsic robustness against experimental imperfections with the high sensitivity near the critical point. This feature can be illustrated by comparing

our protocol with the conventional Rabi measurement method [2], which aims to estimate the amplitude of the signal field by directly coupling it to a qubit. As detailed in the Supplemental Material, the measurement error is proportional to the timing error. In distinct contrast, the present protocol is robust against imperfect timing. As illustrated in Fig. 2(d), within the working regime the dependence of the probability P_e on ε is insensitive to k , which determines the ramping time T . We further confirm this robustness by directly displaying P_e as a function of T for different values of ε , simulated with the master equation (see Sec. S8 of the Supplemental Material). We also note that P_e is insensitive to the frequency fluctuation of the signal field, as shown in Fig. S2(b).

IV. DISCUSSION

In conclusion, we have theoretically proposed and experimentally demonstrated a scheme for realizing a criticality-enhanced quantum sensing protocol. The critical system comprises a qubit and a photonic field stored in a resonator. Under the driving of the signal field, the system has a unique dark eigenstate, where the qubit's excitation number is used as the indicator for estimating the signal field amplitude. The performance of the sensor is insensitive to leakage to the bright states, caused by non-adiabaticity and dissipation, as the qubit is in the same state at the critical point, no matter the system is

in the dark or bright states. We demonstrate our critical sensing protocol with a circuit QED architecture. It should be noted that the criticality-enhanced sensitivity is achieved only when the field amplitude is within a narrow region below the critical point. For the general case, the critical sensing needs to be realized in a two-step procedure, where a rough estimation is first made, following which the field amplitude is shifted to the desired critical region for fine measurement [31]. The working region of the sensor can be broadened by using a tunable coupler [50], with which the qubit-resonator coupling is tunable so that the critical sensor can be adapted for a broader range of the field amplitude. Our approach can be directly applied to other spin-boson systems, e.g., ion traps (see Sec. S10), where the qubit can be better controlled and measured with a higher fidelity [51].

High-precision estimation of the amplitude of a driving field is crucial for implementation of high-fidelity single-qubit gates (see Sec. S11), which are realized by driving the relevant qubits with external fields with well controlled amplitudes. These gates are essential for implementation of quantum algorithms [52] and for multi-qubit quantum state reconstructions [53]. High-precision calibration of the driving amplitude is also crucial for continuous-variable-based quantum information processing protocols with photonic fields [54], where high-precision calibration of external driving fields is crucial for high-fidelity manipulation and readout of the photonic qubits.

-
- [1] B. P. A. et al. (LIGO Scientific and Virgo Collaborations), Observation of gravitational waves from a binary black hole merger, *Phys. Rev. Lett.* **116**, 061102 (2016).
 - [2] C. L. Degen, F. Reinhard, and P. Cappellaro, Quantum sensing, *Rev. Mod. Phys.* **89**, 035002 (2017).
 - [3] D. Braun, G. Adesso, F. Benatti, R. Floreanini, U. Marzolino, M. W. Mitchell, and S. Pirandola, Quantum-enhanced measurements without entanglement, *Rev. Mod. Phys.* **90**, 035006 (2018).
 - [4] A. Facon, E.-K. Dietsche, D. Grosso, S. Haroche, J.-M. Raimond, M. Brune, and S. Gleyzes, A sensitive electrometer based on a Rydberg atom in a Schrödinger-cat state, *Nature (London)* **535**, 262 (2016).
 - [5] K. C. McCormick, J. Keller, S. C. Burd, D. J. Wineland, A. C. Wilson, and D. Leibfried, Quantum-enhanced sensing of a single-ion mechanical oscillator, *Nature (London)* **572**, 86 (2019).
 - [6] W. Wang, Y. Wu, Y. Ma, W. Cai, L. Hu, X. Mu, Y. Xu, Z.-J. Chen, H. Wang, Y. P. Song, H. Yuan, C.-L. Zou, L.-M. Duan, and L. Sun, Heisenberg-limited single-mode quantum metrology in a superconducting circuit, *Nat. Commun.* **10**, 4382 (2019).
 - [7] T. Nagata, R. Okamoto, J. L. O'Brien, K. Sasaki, and S. Takeuchi, Beating the standard quantum limit with four-entangled photons, *Science* **316**, 726 (2007).
 - [8] D. Leibfried, M. D. Barrett, T. Schaetz, J. Britton, J. Chiaverini, W. M. Itano, J. D. Jost, C. Langer, and D. J. Wineland, Toward heisenberg-limited spectroscopy with multiparticle entangled states, *Science* **304**, 1476 (2004).
 - [9] T. Monz, P. Schindler, J. T. Barreiro, M. Chwalla, D. Nigg, W. A. Coish, M. Harlander, W. Hänsel, M. Hennrich, and R. Blatt, 14-qubit entanglement: Creation and coherence, *Phys. Rev. Lett.* **106**, 130506 (2011).
 - [10] G. P. Greve, C. Luo, B. Wu, and J. K. Thompson, Entanglement-enhanced matter-wave interferometry in a high-finesse cavity, *Nature (London)* **610**, 472 (2022).
 - [11] L. Pezzè, Y. Li, W. Li, and A. Smerzi, Witnessing entanglement without entanglement witness operators, *Proc. Natl. Acad. Sci. U.S.A.* **113**, 11459 (2016).
 - [12] S. Sachdev, *Quantum Phase Transitions*, 2nd ed. (Cambridge University Press, 2011).
 - [13] P. Zanardi and N. Paunković, Ground state overlap and quantum phase transitions, *Phys. Rev. E* **74**, 031123 (2006).
 - [14] A. F. Albuquerque, F. Alet, C. Sire, and S. Capponi, Quantum critical scaling of fidelity susceptibility, *Phys. Rev. B* **81**, 064418 (2010).
 - [15] T.-L. Wang, L.-N. Wu, W. Yang, G.-R. Jin, N. Lambert, and F. Nori, Quantum fisher information as a signature of the superradiant quantum phase transition, *New J. Phys.* **16**, 063039 (2014).
 - [16] W.-L. You, Y.-W. Li, and S.-J. Gu, Fidelity, dynamic structure factor, and susceptibility in critical phenomena, *Phys. Rev. E* **76**, 022101 (2007).
 - [17] P. Zanardi, M. G. A. Paris, and L. Campos Venuti, Quan-

- tum criticality as a resource for quantum estimation, *Phys. Rev. A* **78**, 042105 (2008).
- [18] M. Tsang, Quantum transition-edge detectors, *Phys. Rev. A* **88**, 021801 (2013).
- [19] C. Invernizzi, M. Korbman, L. Campos Venuti, and M. G. A. Paris, Optimal quantum estimation in spin systems at criticality, *Phys. Rev. A* **78**, 042106 (2008).
- [20] S. Gammelmark and K. Mølmer, Phase transitions and heisenberg limited metrology in an ising chain interacting with a single-mode cavity field, *New J. Phys.* **13**, 053035 (2011).
- [21] P. A. Ivanov and D. Porras, Adiabatic quantum metrology with strongly correlated quantum optical systems, *Phys. Rev. A* **88**, 023803 (2013).
- [22] G. Salvatori, A. Mandarino, and M. G. A. Paris, Quantum metrology in lipkin-meshkov-glick critical systems, *Phys. Rev. A* **90**, 022111 (2014).
- [23] M. Bina, I. Amelio, and M. G. A. Paris, Dicke coupling by feasible local measurements at the superradiant quantum phase transition, *Phys. Rev. E* **93**, 052118 (2016).
- [24] M. M. Rams, P. Sierant, O. Dutta, P. Horodecki, and J. Zakrzewski, At the limits of criticality-based quantum metrology: Apparent super-heisenberg scaling revisited, *Phys. Rev. X* **8**, 021022 (2018).
- [25] S. Wald, S. V. Moreira, and F. L. Semião, In- and out-of-equilibrium quantum metrology with mean-field quantum criticality, *Phys. Rev. E* **101**, 052107 (2020).
- [26] I. Frérot and T. Roscilde, Quantum critical metrology, *Phys. Rev. Lett.* **121**, 020402 (2018).
- [27] L. Garbe, M. Bina, A. Keller, M. G. A. Paris, and S. Felicetti, Critical quantum metrology with a finite-component quantum phase transition, *Phys. Rev. Lett.* **124**, 120504 (2020).
- [28] A. Niezgoda and J. Chwedeńczuk, Many-body nonlocality as a resource for quantum-enhanced metrology, *Phys. Rev. Lett.* **126**, 210506 (2021).
- [29] L. Garbe, O. Abah, S. Felicetti, and R. Puebla, Critical quantum metrology with fully-connected models: from heisenberg to kibble–zurek scaling, *Quantum Sci. Technol.* **7**, 035010 (2022).
- [30] K. Chen, J. Lü, X. Zhu, H. Zhang, W. Ning, Z. Yang, and S. Zheng, Critical Sensing with a Single Bosonic Mode Without Boson–Boson Interactions, *Adv. Quantum Technol.* , 2400105 (2024).
- [31] R. Liu, Y. Chen, M. Jiang, X. Yang, Z. Wu, Y. Li, H. Yuan, X. Peng, and J. Du, Experimental critical quantum metrology with the Heisenberg scaling, *npj Quantum Inf.* **7**, 170 (2021).
- [32] D.-S. Ding, Z.-K. Liu, B.-S. Shi, G.-C. Guo, K. Mølmer, and C. S. Adams, Enhanced metrology at the critical point of a many-body Rydberg atomic system, *Nat. Phys.* **18**, 1447 (2022).
- [33] M. Raghunandan, J. Wrachtrup, and H. Weimer, High-density quantum sensing with dissipative first order transitions, *Phys. Rev. Lett.* **120**, 150501 (2018).
- [34] T. L. Heugel, M. Biondi, O. Zilberberg, and R. Chitra, Quantum transducer using a parametric driven-dissipative phase transition, *Phys. Rev. Lett.* **123**, 173601 (2019).
- [35] S. Fernández-Lorenzo and D. Porras, Quantum sensing close to a dissipative phase transition: Symmetry breaking and criticality as metrological resources, *Phys. Rev. A* **96**, 013817 (2017).
- [36] T. Ilias, D. Yang, S. F. Huelga, and M. B. Plenio, Criticality-enhanced quantum sensing via continuous measurement, *PRX Quantum* **3**, 010354 (2022).
- [37] R. Di Candia, F. Minganti, K. V. Petrovnin, G. S. Paraoanu, and S. Felicetti, Critical parametric quantum sensing, *npj Quantum Inf.* **9**, 23 (2023).
- [38] Y. Chu, S. Zhang, B. Yu, and J. Cai, Dynamic framework for criticality-enhanced quantum sensing, *Phys. Rev. Lett.* **126**, 010502 (2021).
- [39] J.-H. Lü, W. Ning, X. Zhu, F. Wu, L.-T. Shen, Z.-B. Yang, and S.-B. Zheng, Critical quantum sensing based on the jaynes-cummings model with a squeezing drive, *Phys. Rev. A* **106**, 062616 (2022).
- [40] X. Zhu, J.-H. Lü, W. Ning, F. Wu, L.-T. Shen, Z.-B. Yang, and S.-B. Zheng, Criticality-enhanced quantum sensing in the anisotropic quantum Rabi model, *Sci. China Phys. Mech. Astron.* **66**, 250313 (2023).
- [41] G. Mihailescu, A. Bayat, S. Campbell, and A. K. Mitchell, Multiparameter critical quantum metrology with impurity probes, [arXiv:2311.16931](https://arxiv.org/abs/2311.16931).
- [42] K. Gietka, L. Ruks, and T. Busch, Understanding and Improving Critical Metrology. Quenching Superradiant Light-Matter Systems Beyond the Critical Point, *Quantum* **6**, 700 (2022).
- [43] E. Jaynes and F. Cummings, Comparison of quantum and semiclassical radiation theories with application to the beam maser, *Proc. IEEE* **51**, 89 (1963).
- [44] P. Alsing, D.-S. Guo, and H. J. Carmichael, Dynamic stark effect for the jaynes-cummings system, *Phys. Rev. A* **45**, 5135 (1992).
- [45] J. B. Curtis, I. Boettcher, J. T. Young, M. F. Maghrebi, H. Carmichael, A. V. Gorshkov, and M. Foss-Feig, Critical theory for the breakdown of photon blockade, *Phys. Rev. Res.* **3**, 023062 (2021).
- [46] H. J. Carmichael, Breakdown of photon blockade: A dissipative quantum phase transition in zero dimensions, *Phys. Rev. X* **5**, 031028 (2015).
- [47] J. M. Fink, A. Dombi, A. Vukics, A. Wallraff, and P. Domokos, Observation of the photon-blockade breakdown phase transition, *Phys. Rev. X* **7**, 011012 (2017).
- [48] See Supplemental Material for theoretical and experimental details, which includes Refs. [2,27,51-53,55-62].
- [49] Q. Guo, S.-B. Zheng, J. Wang, C. Song, P. Zhang, K. Li, W. Liu, H. Deng, K. Huang, D. Zheng, X. Zhu, H. Wang, C.-Y. Lu, and J.-W. Pan, Dephasing-insensitive quantum information storage and processing with superconducting qubits, *Phys. Rev. Lett.* **121**, 130501 (2018).
- [50] F. Yan, P. Krantz, Y. Sung, M. Kjaergaard, D. L. Campbell, T. P. Orlando, S. Gustavsson, and W. D. Oliver, Tunable coupling scheme for implementing high-fidelity two-qubit gates, *Phys. Rev. Appl.* **10**, 054062 (2018).
- [51] D. J. Wineland, Nobel lecture: Superposition, entanglement, and raising schrödinger’s cat, *Rev. Mod. Phys.* **85**, 1103 (2013).
- [52] M. A. Nielsen and I. L. Chuang, *Quantum Computation and Quantum Information: 10th Anniversary Edition*, 10th ed. (Cambridge University Press, USA, 2011).
- [53] C. Song, K. Xu, W. Liu, C.-p. Yang, S.-B. Zheng, H. Deng, Q. Xie, K. Huang, Q. Guo, L. Zhang, P. Zhang, D. Xu, D. Zheng, X. Zhu, H. Wang, Y.-A. Chen, C.-Y. Lu, S. Han, and J.-W. Pan, 10-qubit entanglement and parallel logic operations with a superconducting circuit, *Phys. Rev. Lett.* **119**, 180511 (2017).
- [54] B. Vlastakis, G. Kirchmair, Z. Leghtas, S. E. Nigg, L. Frunzio, S. M. Girvin, M. Mirrahimi, M. H. De-

- voret, and R. J. Schoelkopf, Deterministically Encoding Quantum Information Using 100-Photon Schrödinger Cat States, *Science* **342**, 607 (2013).
- [55] C. Song, S.-B. Zheng, P. Zhang, K. Xu, L. Zhang, Q. Guo, W. Liu, D. Xu, H. Deng, K. Huang, D. Zheng, X. Zhu, and H. Wang, Continuous-variable geometric phase and its manipulation for quantum computation in a superconducting circuit, *Nat. Commun.* **8**, 1061 (2017).
- [56] W. Ning, X.-J. Huang, P.-R. Han, H. Li, H. Deng, Z.-B. Yang, Z.-R. Zhong, Y. Xia, K. Xu, D. Zheng, and S.-B. Zheng, Deterministic entanglement swapping in a superconducting circuit, *Phys. Rev. Lett.* **123**, 060502 (2019).
- [57] R.-H. Zheng, W. Ning, Y.-H. Chen, J.-H. Lü, L.-T. Shen, K. Xu, Y.-R. Zhang, D. Xu, H. Li, Y. Xia, F. Wu, Z.-B. Yang, A. Miranowicz, N. Lambert, D. Zheng, H. Fan, F. Nori, and S.-B. Zheng, Observation of a superradiant phase transition with emergent cat states, *Phys. Rev. Lett.* **131**, 113601 (2023).
- [58] K. Xu, Z.-H. Sun, W. Liu, Y.-R. Zhang, H. Li, H. Dong, W. Ren, P. Zhang, F. Nori, D. Zheng, H. Fan, and H. Wang, Probing dynamical phase transitions with a superconducting quantum simulator, *Sci. Adv.* **6**, eaba4935 (2020).
- [59] M. Hofheinz, H. Wang, M. Ansmann, R. C. Bialczak, E. Lucero, M. Neeley, A. D. O'Connell, D. Sank, J. Wenner, J. M. Martinis, and A. N. Cleland, Synthesizing arbitrary quantum states in a superconducting resonator, *Nature* **459**, 546 (2009).
- [60] C. Monroe, D. M. Meekhof, B. E. King, W. M. Itano, and D. J. Wineland, Demonstration of a fundamental quantum logic gate, *Phys. Rev. Lett.* **75**, 4714 (1995).
- [61] D. M. Meekhof, C. Monroe, B. E. King, W. M. Itano, and D. J. Wineland, Generation of nonclassical motional states of a trapped atom, *Phys. Rev. Lett.* **76**, 1796 (1996).
- [62] M. Mohseni, A. T. Rezakhani, and D. A. Lidar, Quantum-process tomography: Resource analysis of different strategies, *Phys. Rev. A* **77**, 032322 (2008).

ACKNOWLEDGMENTS

Funding: This work was supported by the National Natural Science Foundation of China under (Grants No. 12474356, No. 12475015, No. 12274080, No. 12174058, No. 11875108, No. 12204105), and Innovation Program for Quantum Science and Technology under Grant No. 2021ZD0300200.

Competing interests: Authors declare that they have no competing interests.

Data and materials availability: All data are available in the main text or the supplementary materials.

Supplementary Materials for
Critical quantum metrology robust against dissipation and
non-adiabaticity

Jia-Hao Lü *et al.*

Corresponding author: Zhen-Biao Yang, zbyang@fzu.edu.cn; Huai-Zhi Wu,
huaizhi.wu@fzu.edu.cn; Shi-Biao Zheng, t96034@fzu.edu.cn

This PDF file includes:

- **Supplementary Text**
- **Figs. S1 to S15**
- **References**

S1. FISHER INFORMATION OF THE DRIVEN JAYNES-CUMMINGS MODEL

The population of the excited state $|e\rangle$ is defined as the expectation value of the excitation-number operator $P_e = \langle |e\rangle \langle e| \rangle$. In the two-level approximation, the operator $|e\rangle \langle e|$ can be rewritten as $|e\rangle \langle e| = \frac{1}{2}(I + \sigma_z)$, where I denotes the identity operator and $\sigma_z = |e\rangle \langle e| - |g\rangle \langle g|$. Then the standard deviation of P_e is given by

$$\Delta P_e = \frac{1}{2} \sqrt{\langle (1 + \sigma_z)^2 \rangle - \langle 1 + \sigma_z \rangle^2} = \frac{1}{2} \sqrt{1 - \langle \sigma_z \rangle^2}. \quad (\text{S1})$$

Using the expression $\langle \sigma_z \rangle = 2P_e - 1$, we obtain

$$\Delta P_e = \frac{1}{2} \sqrt{1 - (2P_e - 1)^2} = \sqrt{P_e(1 - P_e)}. \quad (\text{S2})$$

For the dark state $|\phi_0\rangle$, $P_e = |c_-|^2 = \frac{1}{2}(1 - \sqrt{1 - \varepsilon^2})$. Substituting P_e into the above expression, we obtain $\Delta P_e = \varepsilon/2$. The corresponding Fisher information is defined as

$$\mathcal{F} = \frac{1}{P_e} \left(\frac{dP_e}{d\varepsilon} \right)^2 + \frac{1}{P_g} \left(\frac{dP_g}{d\varepsilon} \right)^2, \quad (\text{S3})$$

and is adopted in the main text. In the two-level approximation, $P_e + P_g = 1$. Then \mathcal{F} can be re-expressed as

$$\mathcal{F} = \left(\frac{1}{P_e} + \frac{1}{1 - P_e} \right) \left(\frac{dP_e}{d\varepsilon} \right)^2 = \frac{1}{P_e(1 - P_e)} \left(\frac{dP_e}{d\varepsilon} \right)^2. \quad (\text{S4})$$

Using $dP_e/d\varepsilon = \varepsilon/(2\sqrt{1 - \varepsilon^2})$, we finally have

$$\mathcal{F} = \frac{1}{1 - \varepsilon^2}. \quad (\text{S5})$$

On the other hand, the quantum Fisher information is [S1]

$$\mathcal{I} = 4[\langle \partial_\varepsilon \phi_0 | \partial_\varepsilon \phi_0 \rangle + \langle \partial_\varepsilon \phi_0 | \phi_0 \rangle^2] = \frac{1}{1 - \varepsilon^2}, \quad (\text{S6})$$

which implies that the Cramér-Rao bound is saturated for all values of ε for our experimental measurements.

S2. NUMERICAL SIMULATIONS OF THE DRIVEN JAYNES-CUMMINGS MODEL

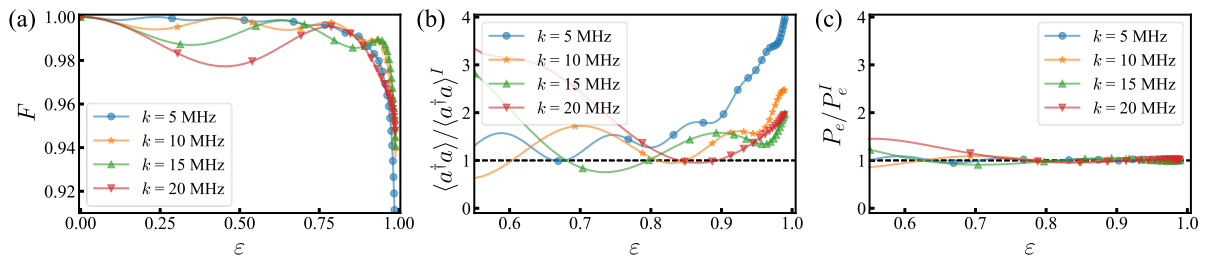


FIG. S1. The numerical simulations based on the master equation. (a) Fidelities evolutions of the dark state as a function of ε . The ratio of the measured (b) average photon number as well as the (c) qubit's excitation number to that in the ideal dark state, versus the control parameter ε for different k , where $\langle a^\dagger a \rangle^I$ and P_e^I denote the average photon number and the $|e\rangle$ -state population of the ideal dark state, respectively.

In order to quantify the effect of the decoherence and non-adiabatic transitions, we here describe the dynamics by the Lindblad master equation

$$\dot{\rho} = -i[H, \rho] + \kappa_q \mathcal{L}[\sigma_-] + \gamma_q \mathcal{L}[|e\rangle \langle e|] + \kappa_r \mathcal{L}[a], \quad (\text{S7})$$

where H is given by Eq. (1) of the main text with $\Omega = 2\pi \times 20.9$ MHz, and the Lindblad superoperators are defined as

$$\mathcal{L}[O] = O\rho O^\dagger - \frac{1}{2}O^\dagger O\rho - \frac{1}{2}\rho O^\dagger O. \quad (\text{S8})$$

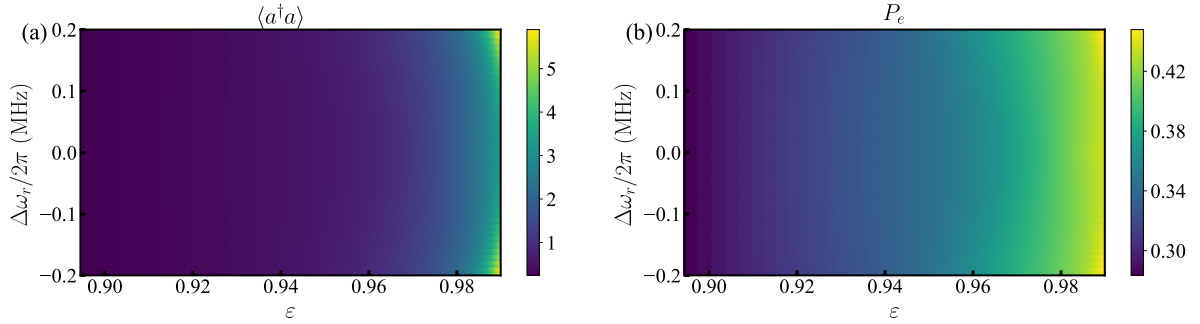


FIG. S2. The numerical simulations of (a) the average photon number and (b) the qubit's excitation number versus the detuning of the signal field with respect to the resonator frequency.

The energy decaying rates for the qubit and the resonator are $\kappa_q = 0.05$ MHz and $\kappa_r = 0.08$ MHz respectively, and $\gamma_q = 0.08$ MHz is the dephasing rate of the qubit.

We then perform the numerical simulations on the ratio of the measured average photon number as well as the qubit's excitation number to that in the ideal dark state, versus the control parameter ε . These ratios, together with the fidelity evolutions of the dark state, are presented in Fig. S1, which shows that, as $\varepsilon \rightarrow 1$, the probability of leakage to the bright state increases dramatically, as a consequence of the decoherence and non-adiabatic effect. Owing to the high distinction of the average photon number between the ideal dark state and the bright state, the measured average photon number is sensitive to the state leakage. In distinct contrast, when approaching the critical point, the qubit's excitation number of the ideal dark state tends to be $1/2$, which is consistent with the bright state. This implies that the qubit's excited-state population (P_e) is insensitive to leakage to the bright state, making it qualified to serve as a robust indicator for quantum sensing.

Although the dark state is obtained under the resonant condition, P_e is insensitive to the frequency fluctuations. To illustrate this point, we perform a numerical simulation to quantify the effect of a frequency deviation $\Delta\omega_r = \omega_r - \omega_s$ of the signal field. As shown in Fig. S2, P_e is robust to the slight frequency detuning of the signal field, which further verifies the robustness of the sensing protocol.

It should be noted that P_e becomes increasingly sensitive to the ramping speed when ε is approaching the critical point, where the energy gaps are closed. The smaller the ramping speed which is determined by k , the better the adiabatic condition being satisfied. However, the increase of the time would cause more serious decoherence. Therefore, there is a trade-off between the non-adiabaticity and decoherence.

For certain coherence times, the optimal ramping speed depends on the choice of the working point, ε_w , around which the control parameter ε is assumed to be. In Fig. S3(a), we present the relative error of P_e , defined as $D = |P_e - P_e^I|/P_e^I$, as a function of ε_w and k for the decaying rates of our systems: $\kappa_q = 0.05$ MHz and $\kappa_r = 0.08$ MHz. Here k determines the ramping speed, as shown in Eq. (5) of the main text. The dots represent the points where the errors are not larger than 0.1%. As this upper bound is much smaller than the error caused by the parameter fluctuation in our system, the value of k at each of such points can be reasonably taken as the optimal value for the corresponding working point ε_w . In our experiment, we choose $k = 10$ MHz, which represents an optimal value for $\varepsilon_w = 0.98$. For this working point, there exist other optimal values of k larger than 10 MHz. However, due to the limitation of the anharmonicity of the qubit in our circuit QED system, larger ramping speeds may incur more serious leakage to the qubit's third level. Figure S3(b)-(d) show D versus ε_w and k for other values of the decaying rates.

S3. NUMERICAL SIMULATIONS OF THE DRIVEN XMON-RESONATOR SYSTEM

In this section, we focus mainly on the influence brought about by the energy levels higher than the first excited state $|e\rangle$ of the qubit. In this case, the Lindblad master equation can be rewritten as

$$\begin{aligned} \dot{\rho} &= -i[H_{full}, \rho] + \kappa_q \mathcal{L}[q] + \gamma_q \mathcal{L}[q^\dagger q] + \kappa_r \mathcal{L}[a], \\ H_{full} &= \omega_r a^\dagger a + \omega_e q^\dagger q - \frac{\chi}{2} q^{\dagger 2} q^2 + \Omega[(a^\dagger q + a q^\dagger) + \varepsilon(a^\dagger e^{-i\omega_s t} + a e^{i\omega_s t})/2], \end{aligned} \quad (S9)$$

where q^\dagger (q) and a^\dagger (a) denote the creation (annihilation) operator for the Xmon qubit and the resonator respectively, and χ is the anharmonicity for qubit's level ladder; ω_e is the transition frequency between $|g\rangle$ and $|e\rangle$ and ω_r represents the resonator's frequency; ε characterizes the rescaled amplitude of the microwave field coupled to the photonic mode with the frequency ω_s .

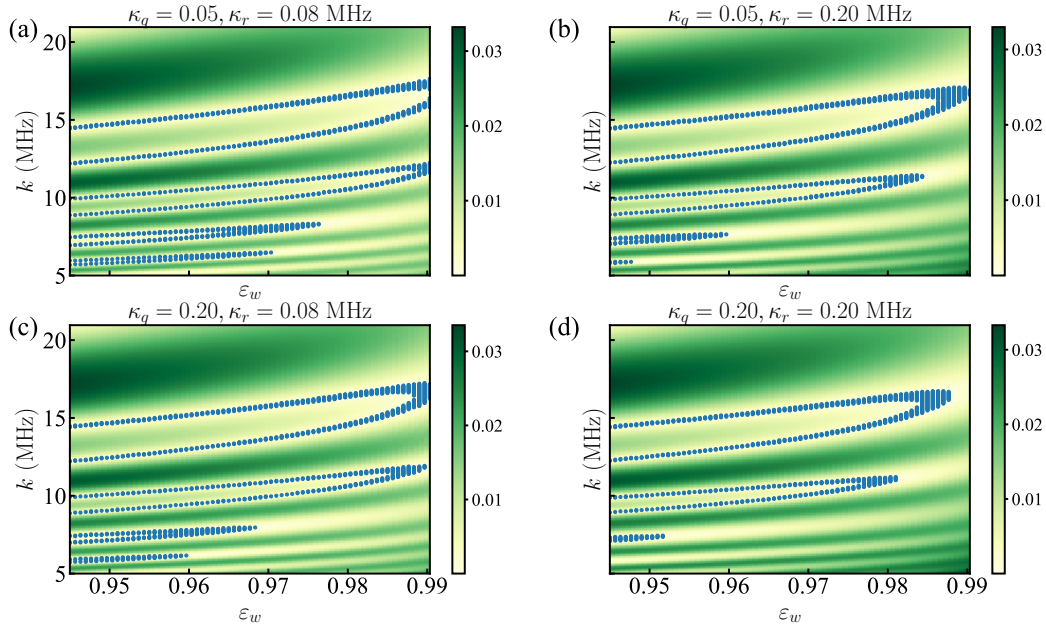


FIG. S3. Relative deviation of P_e from the ideal value versus ε_w and k for different decaying rates.

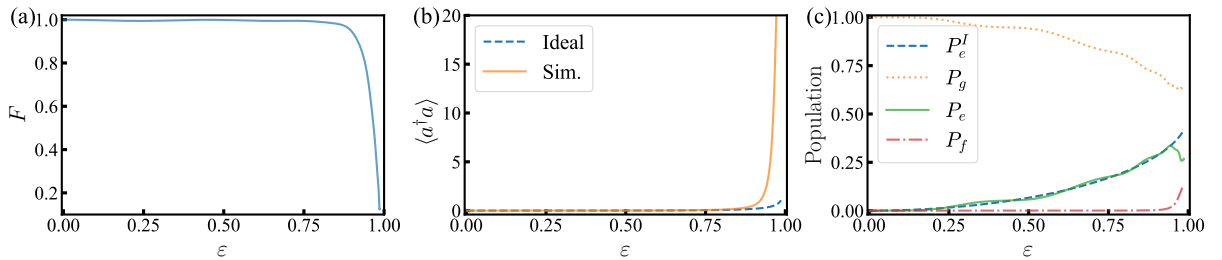


FIG. S4. The numerical simulations based on the Hamiltonian of Eq. (S10). (a) Fidelity of the qubit-resonator state to the ideal dark state as a function of ε . (b) The average photon number and (c) the qubit's population distribution as a function of ε . P_e^I denotes the $|e\rangle$ -state population of the ideal dark state. In the simulation, the parameters are the same as that shown in the main text.

For simplicity, we include only the second excited state $|f\rangle$, while we note that the influences of the higher excited states on the system's dynamics are slight and can be neglected compared to $|f\rangle$. The Hamiltonian for the driven qutrit-resonator system is given by (setting $\hbar = 1$)

$$H' = \omega_e |e\rangle\langle e| + (2\omega_e - \chi) |f\rangle\langle f| + \omega_r a^\dagger a + \Omega \left[a^\dagger \left(|g\rangle\langle e| + \sqrt{2} |e\rangle\langle f| + \frac{\varepsilon}{2} e^{-i\omega_s t} \right) + \text{H.c.} \right], \quad (\text{S10})$$

We then perform the numerical simulations based on the Hamiltonian H' in Eq. (S10). As shown in Fig. S4, when the resonator couples resonantly with both the qubit and the microwave field, the system's dynamics deviates significantly from the desired one when approaching the critical point, where the infidelity for the ideal dark state increases exponentially. Additionally, the average photon number exhibits a behavior that is very different from the ideal one near the critical point, owing to the large leakage to the bright states. Although the qubit's $|e\rangle$ -state population is insensitive to the leakage to the bright states in the two-level approximation, it presents an undesirable behavior near the critical point where the population of the $|f\rangle$ -state increases to 0.13. As shown in Fig. S4(c), the non-negligible influence of the $|f\rangle$ -state breaks down the monotonous feature of the $|e\rangle$ -state population near the critical point.

S4. SUPPRESSION OF LEAKAGE TO THE SECOND-EXCITED STATE OF THE XMON

To make the sensor work near the critical point, it is necessary to suppress the population of the second excited state of the Xmon. We find that this can be significantly optimized by fine tuning the detunings of the Xmon and

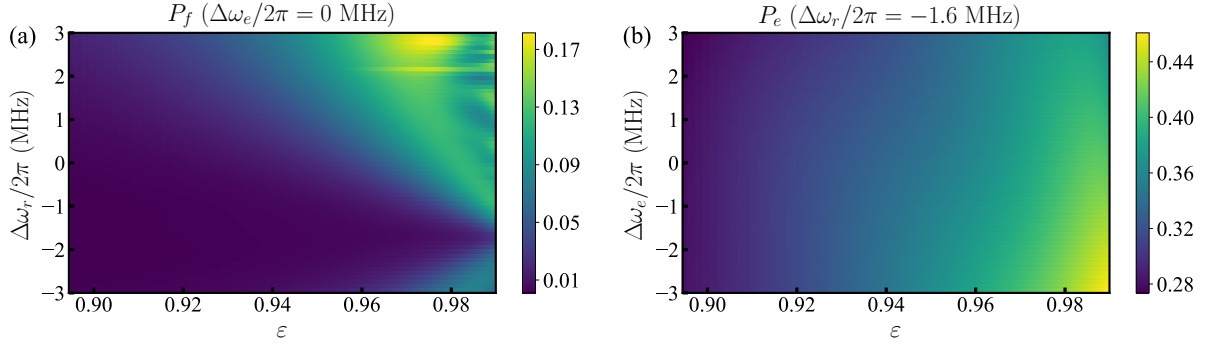


FIG. S5. The numerical simulations with the fine-tuned frequency detunings. (a) The qubit's $|f\rangle$ -state population versus the detuning of the resonator to the signal field during the evolution. It shows that the probability of leaking to the state $|f\rangle$ can be highly suppressed at a specific detuning. We here set the detuning between the qubit and the signal field to zero. (b) The qubit's $|e\rangle$ -state population versus the detuning of the qubit to the signal field. The detuning between the resonator and the microwave field is chosen as $-2\pi \times 1.6$ MHz. The other parameters are the same as shown above.

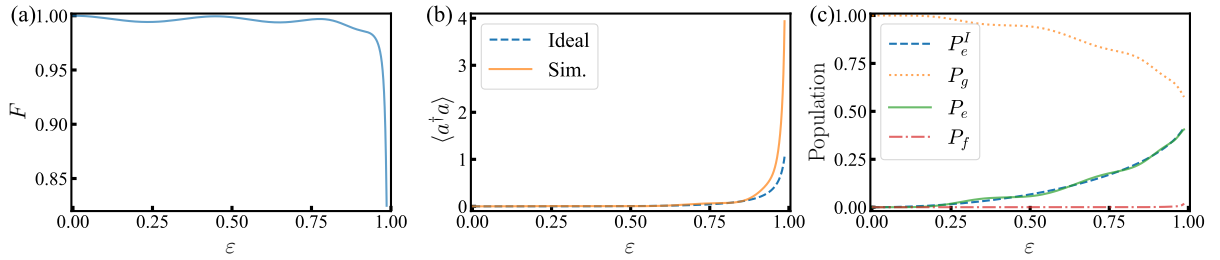


FIG. S6. The numerical simulations with the chosen frequency detunings. (a) Fidelity of the qubit-resonator state to the ideal dark state versus ε . (b) The average photon number and (c) the qubit's population distribution versus ε . P_e^I denotes the $|e\rangle$ -state population of the ideal dark state. In the simulation, the detunings of the resonator and the qubit with respect to the signal field are tuned to $-2\pi \times 1.6$ MHz and $2\pi \times 1.0$ MHz, respectively. The other parameters are the same as shown above.

the resonator from the signal field. With the detunings being included, the system Hamiltonian in the framework rotating at the frequency of the signal field is

$$H'_I = \Delta\omega_e|e\rangle\langle e| + (2\Delta\omega_e - \chi)|f\rangle\langle f| + \Delta\omega_r a^\dagger a + \Omega \left[a^\dagger \left(|g\rangle\langle e| + \sqrt{2}|e\rangle\langle f| + \frac{\varepsilon}{2} \right) + \text{H.c.} \right], \quad (\text{S11})$$

where $\Delta\omega_r = \omega_r - \omega_s$ and $\Delta\omega_e = \omega_e - \omega_s$ are the detunings of the resonator and the qubit with respect to the signal field, respectively.

We then perform the numerical simulations by tuning $\Delta\omega_r$ and $\Delta\omega_e$ successively, as exhibited in Fig. S5, which shows that the probability of leaking to the $|f\rangle$ -state can be highly suppressed through the optimization of the frequency detunings, and the $|e\rangle$ -state population agrees well with that of the on-resonance dynamics. Seen from Fig. S5, we note that the set of optimal detunings of the resonator and the qubit with respect to the signal field are $-2\pi \times 1.6$ MHz and $2\pi \times 1.0$ MHz, respectively. With the chosen frequency detunings, when approaching the critical point we find that the fidelity with respect to the effective model remains higher than 0.9 for $\varepsilon = 0.98$; the associated average photon number is greatly reduced as compared to the case without such a frequency adjustment; and more importantly, the probability of leaking to the $|f\rangle$ -state decreases correspondingly such that the qubit's $|e\rangle$ -state population becomes well consistent with the ideal situation, as shown in Fig. S6. In view of experiments, we further fine tune the detunings of the resonator and the qubit around the numerically estimated optimal parameters (i.e. $\Delta\omega_r = -2\pi \times 1.6$ MHz and $\Delta\omega_e = 2\pi \times 1.0$ MHz), making the overall evolution dynamics match the theoretical predictions (as elaborated in the main text).

S5. CORRECTION OF XY CROSSTALK

The superconducting circuit sample used in our experiment consists of five frequency-tunable Xmon qubits interconnected by a bus resonator, as described elsewhere [S2–S4]. Our experiment involves two of the qubits, one of which serves as the test qubit, labeled as Q_T , to establish the critical quantum dynamics together with the bus resonator, and the other, labeled as Q_A , to read out the photon number distribution of the resonator by observing its on-resonance Rabi signal. Additionally, we use the XY-control line of the qubit Q_R to apply a

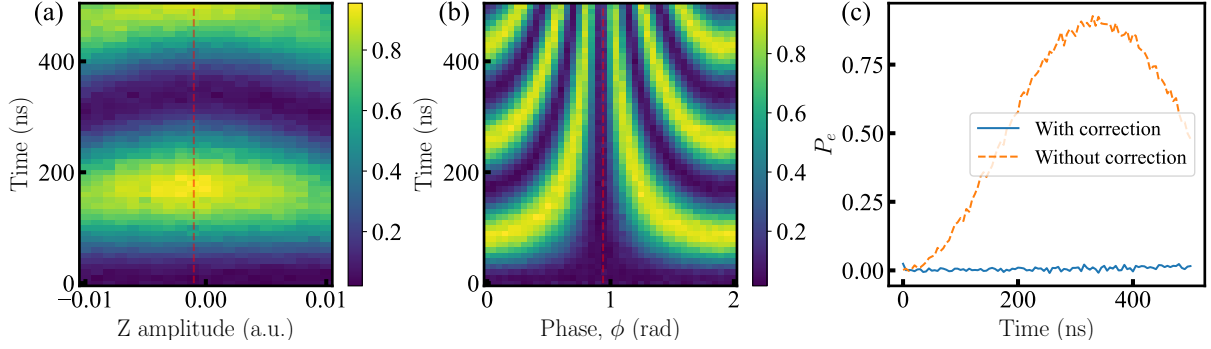


FIG. S7. Correction of the XY-crosstalk. (a) The measurement of the XY-crosstalk amplitude. A microwave pulse with frequency ω_I is applied to Q_R 's XY-control line after tuning Q_T to ω_I , generating a crosstalk Rabi oscillation on Q_T . The Rabi oscillations are measured with small deviation in frequency. The slowest Rabi oscillation corresponds to the crosstalk amplitude, as the red vertical dashed line shows. Here the pulse amplitude is set to $2\pi \times 5$ MHz. (b) The measurement of the XY-crosstalk phase. A microwave pulse with amplitude equal to crosstalk amplitude is added to Q_T 's XY-control line to cancel the crosstalk effect. The phase in which qubit is rarely excited is the crosstalk phase. (c) Experiment test for the crosstalk correction. With the applications of the XY-crosstalk correction, Q_T is barely excited. The pulse amplitude here is set to $2\pi \times 10$ MHz.

microwave drive to the resonator by crosstalk interactions. The remaining qubits are at their sweep points, so as to effectively decouple from the dynamics.

The pulse sequence of our experiment is shown in Fig. S10. When Q_T is tuned to couple resonantly with the resonator, the phase and the drive strength of the XY-drive crosstalks between Q_T and the resonator must be corrected [S5]. Figure S7 illustrates the calibration process for the XY-drive applied to the resonator as an example.

We start by calibrating the amplitude of the crosstalk, with the results shown in Fig. S7(a). For this, Q_T is biased to the frequency $\omega_I/2\pi = 5.53$ GHz, which is close to the resonator's frequency, and the other qubits are decoupled from Q_T and the resonator. It should be emphasised that the reason we are unable to perform the XY crosstalk calibration at the resonator's frequency is that the on-resonance dynamics between Q_T and the resonator complicates the effect of the crosstalk, which makes the crosstalk amplitude extremely difficult to capture. We here assume that a small frequency detuning has no effect on the crosstalk. After that, a strong flat-top-envelope microwave pulse is applied to the Q_R 's XY-control line with frequency ω_I , generating a crosstalk excitation on Q_T . The amplitude of the crosstalk of the resonator to Q_T can be obtained by fitting the slowest Rabi oscillation of the evolution of Q_T 's excitation, resulting from different frequency deviation in ω_I .

We characterize the phase of the crosstalk in terms of the frequency corresponding to the slowest Rabi oscillation in Fig. S7 (b). At this point, a microwave pulse with amplitude equal to the crosstalk amplitude of the resonator to Q_T , should be applied to Q_T to counteract the effect of the crosstalk. We then monitor the evolution of Q_T ' excitation for different phases of Q_T 's microwave pulse, with the π -phase of Q_R 's microwave pulse. As shown in Fig. S7 (b), Q_T is barely excited during the evolution process at a specific phase, meaning the phase difference of the XY-control lines of Q_R to Q_T .

The calibrations of Q_T to Q_R ' XY-control line are performed in the same way. To correct the crosstalks, we bias Q_T/Q_R to ω_I , and simultaneously apply on-resonance microwave pulses to them, with amplitudes A_1/A_2 and phases ϕ_1/ϕ_2 . During the process, the other qubits are effectively decoupled from these two qubits. However, owing to the effect of the crosstalks, the microwave's effect on each qubit at this point becomes

$$\begin{bmatrix} A_1 e^{i\phi_1} + A_{12} A_2 e^{i(\phi_{12} + \phi_2)} \\ A_2 e^{i\phi_2} + A_{21} A_1 e^{i(\phi_{21} + \phi_1)} \end{bmatrix} = \begin{bmatrix} 1 & A_{12} e^{i\phi_{12}} \\ A_{21} e^{i\phi_{21}} & 1 \end{bmatrix} \begin{bmatrix} A_1 e^{i\phi_1} \\ A_2 e^{i\phi_2} \end{bmatrix}, \quad (\text{S12})$$

where A_{jk} and ϕ_{jk} denote the crosstalk amplitude and phase of qubit k to qubit j , respectively, quantified by means of the method described above. This means that, to cancel the effect of the crosstalk, a corrected microwave pulse

$$\begin{bmatrix} 1 & A_{12} e^{i\phi_{12}} \\ A_{21} e^{i\phi_{21}} & 1 \end{bmatrix}^{-1} \begin{bmatrix} A_1 e^{i\phi_1} \\ A_2 e^{i\phi_2} \end{bmatrix}, \quad (\text{S13})$$

should be applied to get the expected microwave pulse.

To ensure the validity of the XY-crosstalk correction, we bias Q_T to ω_I and apply the corresponding calibrated microwave pulses to Q_R and Q_T , respectively. We then observe the evolution of Q_T ' excitation, as displayed in Fig. S7 (c). The result verifies the validity of such a correction.

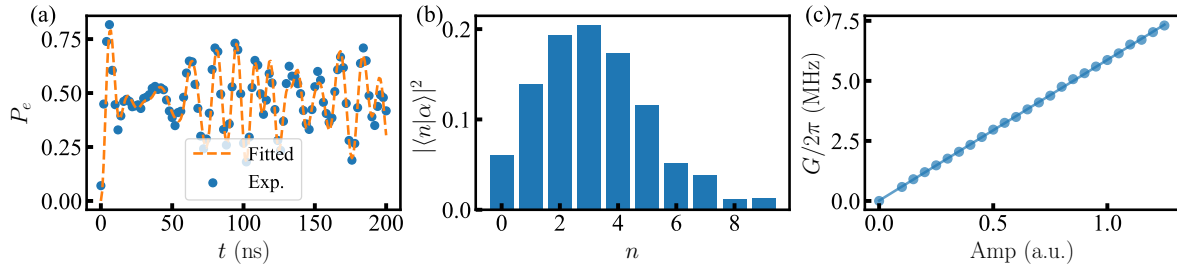


FIG. S8. Calibration of the drive strength of the microwave. (a) The experimental (dots), the fitted (solid line) Rabi oscillations and (b) the corresponding photon-number distribution of the resonator. Here, τ is set to 100 ns with a specific pulse amplitude of the microwave. (c) The drive strength G as a function of the pulse amplitude of the microwave.

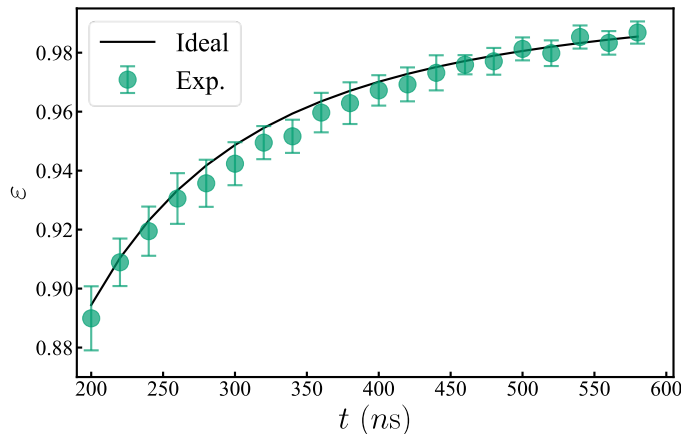


FIG. S9. The measurement of the rescaled driving field strength (ε) of the resonator. The values of ε measured at different times are denoted by the cyan round spots, with the error bars characterizing the fluctuations due to the control imperfections. The black solid line represents the ideal results.

S6. CALIBRATION OF THE SIGNAL FIELD AMPLITUDE

In our experimental protocol, a time-dependent transverse field should be applied to the resonator. It is necessary to calibrate the linear relation between the pulse amplitude of the microwave and the driving field strength of the resonator.

To this end, we first use the XY-control line of Q_R to apply a microwave drive with the amplitude ξ to the resonator by the crosstalk interaction, which produces a equivalent driving field strength G to drive the resonator. After a time τ , the state of the resonator can be described as

$$|R(\tau)\rangle = e^{-iG(a+a^\dagger)\tau}|R(0)\rangle = |\alpha\rangle, \quad (\text{S14})$$

where $|R(0)\rangle = |0\rangle$ denotes the initial state of the resonator, and $\alpha = -iG\tau$ represents the displacement coefficient. The average photon number $|\alpha|^2$ of such a coherent state can then be read out by switching off the drive and tuning Q_A to couple resonantly with the resonator (the details are described in the next part). After that, the corresponding driving field strength $G = |\alpha|/\tau$ can be deduced. A linear connection of the pulse amplitude of the microwave to the driving field strength of the resonator can be naturally fitted through the applications of different pulse amplitude of the microwave, as exhibited in Fig. S8. Figure S9 presents the rescaled driving amplitude measured with our critical sensing protocol. As shown in the numerical simulation of Fig. S1(c), the qubit's excited-state population, which is used as the sensing indicator, is insensitive to both the non-adiabaticity and decoherence effects near the critical point. Therefore, the deviations of the measured field amplitudes from the preset values are mainly due to the fluctuations of the driving field itself.

S7. OBSERVED PHOTON-NUMBER DISTRIBUTION

After the interaction dynamics between the qubit Q_T and the resonator, the transverse field is switched off, so that the qubit is effectively decoupled from the resonator. The photon number distribution of the resonator is read

out by tuning the ancilla qubit Q_A , initially in its ground state, to the resonator frequency, and then observing its Rabi oscillations [S6]. The excited state population $P_e^\varepsilon(\tau)$ of Q_A , after tuning back to its idle frequency, for the rescaled amplitude ε at the evolution time τ is measured, the pulse sequence is shown in Fig. S10. The measured average photon numbers are calculated by the photon-number distribution, which is fitted by the time-dependent Rabi signal as

$$P_e^\varepsilon(\tau) = \frac{1}{2} \left[1 - P_g^\varepsilon(0) \sum_{n=0}^{n_{max}} P_n e^{-\kappa_n \tau} \cos(2\sqrt{n}\Omega_A \tau) \right], \quad (\text{S15})$$

where $P_g^\varepsilon(0)$ denotes the probability for Q_A initially in its ground state, P_n presents the probability for the $|n\rangle$ -state photon-number distribution, n_{max} is the fitted cutoff of the photon number, $\kappa_n = n^l/\kappa_r$ ($l = 0.7$) is the empirical decay rate of the $|n\rangle$ -state Rabi oscillation and Ω_A represents the on-resonance photonic swapping rate between Q_A and the resonator. Here, the ideal dark state of the resonator is a squeezed vacuum state, which means that the high-photon state distribution affects the dynamics markedly, increasing the difficulty of the fitting. The measured time-dependent Rabi oscillation signal and its fitting are shown in Fig. S11(a). The corresponding photon-number distribution is presented in Fig. S11(b).

In Fig. S12, we present the average photon number of the resonator and the $|e\rangle$ -state population of Q_T during the whole dynamics. As expected, the qubit's excitation number is robust against the imperfect system dynamics rather than the average photon number, making P_e serve as an ideal indicator for critical quantum sensing.

S8. COMPARISON WITH RABI MEASUREMENT

It is enlightening to compare our critical protocol with the conventional Rabi measurement method [S7]. The Rabi measurement is realized by coupling the signal field to a qubit [S7]. The dynamics is described by the Hamiltonian

$$H_{Rabi} = \frac{\varepsilon}{2} (|g\rangle \langle e| + |e\rangle \langle g|), \quad (\text{S16})$$

where ε is the amplitude of the signal field. Under this Hamiltonian, the qubit state, initially being $|g\rangle$, evolves as

$$|\psi(t)\rangle = \cos(\theta/2) |g\rangle - i \sin(\theta/2) |e\rangle, \quad (\text{S17})$$

where $\theta = \varepsilon t$. The $|e\rangle$ -state population makes Rabi oscillations, given by

$$P_e = \frac{1}{2} (1 - \cos \theta). \quad (\text{S18})$$

The interferometer works by measuring the deviation of this transition probability from a well-chosen reference point P_0 , referred to as the bias point, corresponding to a known value of the field amplitude (ε_0) and a well-chosen time t . The interferometer is most sensitive to a small deviation ($\delta\varepsilon$) from ε_0 at the point $P_0 = 1/2$, where

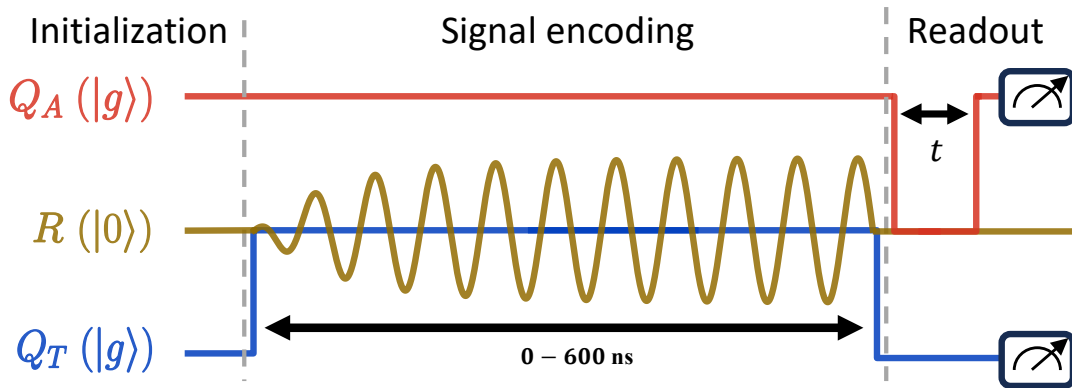


FIG. S10. Pulse sequence. The qubit (Q_T) is tuned from its frequency to the resonator's frequency. At the same time the signal field with a rescaled amplitude ε is coupled to the resonator. After the quench process, the qubit is biased back to its idle frequency for state readout, and the ancilla qubit (Q_A) is tuned to couple resonantly with the resonator to measure the photon-number distribution.

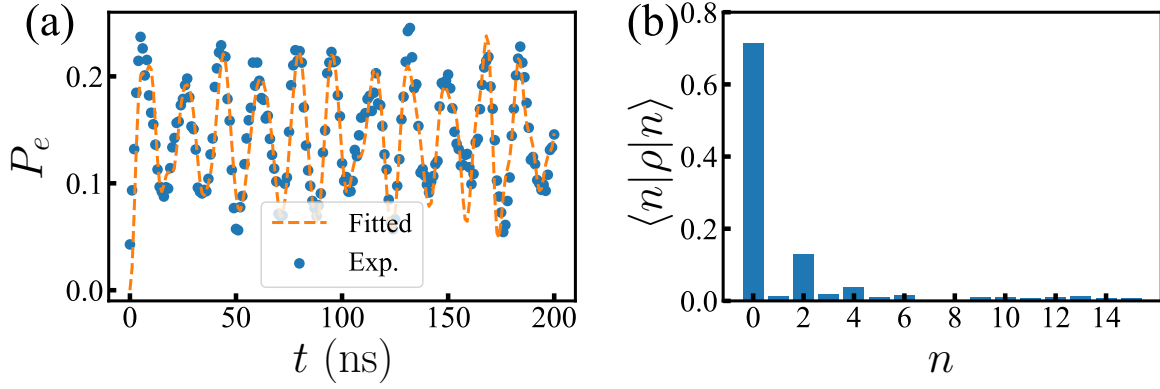


FIG. S11. (a) The experimental (dots), the fitted (solid line) Rabi oscillations and (b) the corresponding photon-number distribution of the resonator with $\varepsilon = 0.964$.

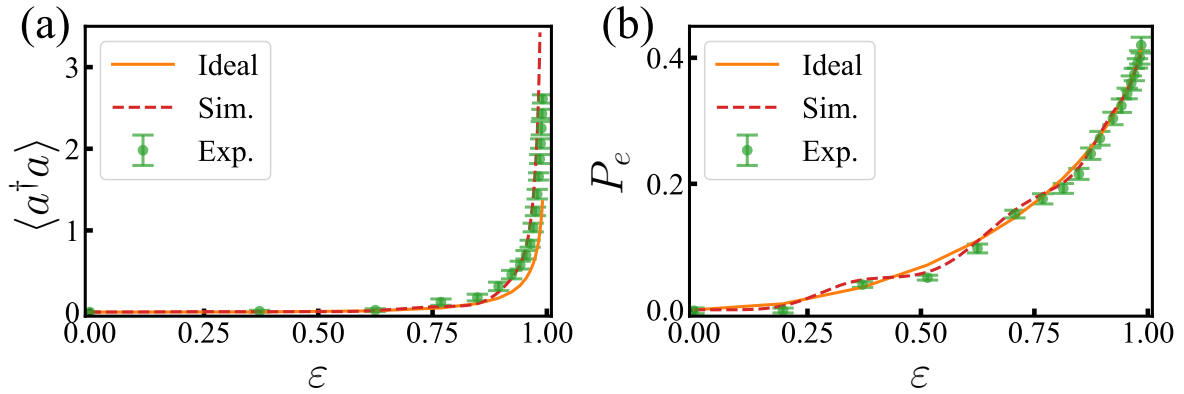


FIG. S12. (a) The experimental average photon number and (b) the $|e\rangle$ -state population as a function of ε during the whole dynamics. The solid lines denote the result of the ideal dark state, and the dashed lines are that for the numerical simulations.

$|dP_e/d\theta|$ has the maximum $1/2$. The bias point corresponds to $\varepsilon_0 t_n = n\pi/2$, where $n = 1, 3, 5, \dots$. Around the bias point, the deviation of P_e from P_0 depends on

$$\Delta P_e = -\frac{1}{2} \cos[(\varepsilon_0 + \delta\varepsilon)t_n] \simeq \frac{1}{2} (-1)^{(n-1)/2} \delta\varepsilon t_n. \quad (\text{S19})$$

The precision of the Rabi measurement method strongly depends upon the accuracy of the timing. Set the deviation of the real time from the desired value (t_n) to be δt_n . The error of the $|e\rangle$ -state population caused by this imperfect timing is given by

$$\delta P_e \simeq \frac{1}{2} (-1)^{(n-1)/2} \varepsilon_0 \delta t_n, \quad (\text{S20})$$

which linearly scales with the time control error δt_n .

The present protocol combines the intrinsic robustness of the adiabatic evolution with the high sensitivity near the critical point, and thus is insensitive to the control error. In our adiabatic protocol, the control parameter ε depends on the time as

$$\varepsilon(t) = \sqrt{1 - (k^2 t^2 + 1)^{-1}}. \quad (\text{S21})$$

The time needed to reach the preset value of ε is determined by k , which controls the ramping velocity. As shown in Fig. 2(d) of the main text, within the working regime the qubit's $|e\rangle$ -state population (P_e) almost remains the same for a wide range of the values of k . This implies that the scheme is robust against imperfect timing. To further confirm this point, we perform a simulation of P_e for different values of the ramping time T . Figure S13 displays P_e versus T for different values of $\varepsilon(T)$. P_e at each point is calculated using the master equation, where the system parameters are the same as those in the text. The result unambiguously demonstrates that P_e is indeed insensitive to the ramping time. For example, for $\varepsilon(T) = 0.985$, P_e falls within the narrow regime $[0.98P_e^I, 1.0P_e^I]$ even when T is ranged from $0.7T^I$ to $1.3T^I$, where P_e^I and T^I denote $|e\rangle$ -state population and

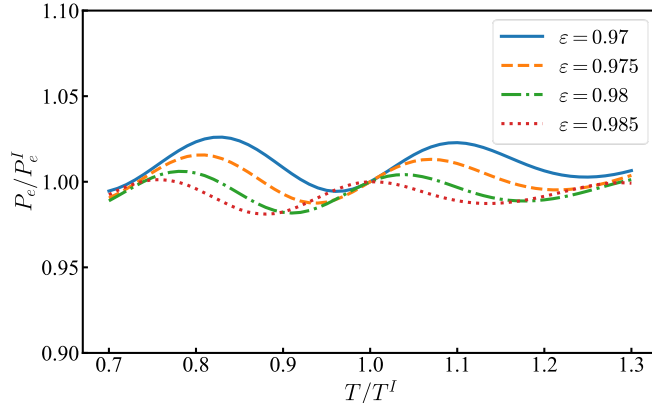


FIG. S13. The qubit's $|e\rangle$ -state population P_e as a function of the ramping time T for specific $\varepsilon(T)$, where P_e^I and T^I denote the simulated results with $k = 10$ MHz. In the simulation, P_e at each point is calculated using the master equation, where the system parameters are the same as those shown in the main text.

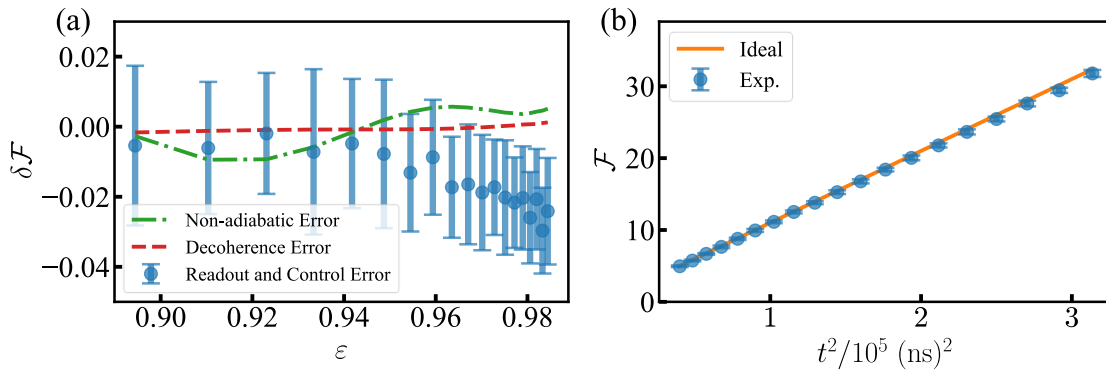


FIG. S14. (a) Errors of \mathcal{F} versus the control parameter ε . The error sources include non-adiabaticity, decoherence, and readout and calibration imperfection. Each error source causes a deviation of the measured \mathcal{F} from the ideal value. The effect of each error source is quantified by the ratio between the resulting deviation and the ideal value. (b) The Fisher information \mathcal{F} versus t^2 .

total time for the simulated results with $k = 10$ MHz, respectively. We note that this robustness is achieved at the price of needing a resonator to realize the JCM, which is unnecessary in the Rabi measurement method.

S9. ERRORS AND SCALING OF THE FISHER INFORMATION

As show in Eq. S4, the Fisher information depends on both the $|e\rangle$ -state population (P_e) of the qubit and its derivative with respect to the control parameter ε . This derivative cannot be directly obtained from the experimental data, which are measured for discrete values of ε . To obtain this derivative at each point, we fit P_e as a function of ε with the measured data, and then calculate the derivative. The error sources of \mathcal{F} include non-adiabaticity, decoherence, readout infidelity, and calibration error. To quantify these errors, we first calculate \mathcal{F} for different values of ε , based on the Hamiltonian dynamics and the master equation, respectively. The difference between the result obtained with the Hamiltonian dynamics and that for the ideal dark state is due to the non-adiabaticity. The deviation of the result based on the master equation from that with the Hamiltonian dynamics originates from the decoherence. The difference between the experimental data and the simulation with the master equation is attributed to the readout error and the fluctuation of the control parameter. We cannot individually quantify these two errors. Fig. S14(a) displays the relative error budgets, defined as the ratios between these deviations and the ideal value of \mathcal{F} , versus ε . These errors can be mitigated by improving the coherence times of the system and readout fidelity, and by suppressing the parameter fluctuation.

It is enlightening to explore the scaling of the Fisher information with the time which can be considered as the sensing resource [S1]. When time dependence of the control parameter ε is given by Eq. (5), the Fisher

information for the ideal dark state linearly scales with the square of the time, given by

$$\mathcal{F} = k^2 t^2 + 1. \quad (\text{S22})$$

This corresponds to the optimal Heisenberg scaling precision [S1]. Figure S14(b) shows the time dependence of the Fisher information obtained from the measured P_e , which well agrees with the ideal result (solid line).

S10. IMPLEMENTATION OF THE METROLOGICAL PROTOCOL IN ION TRAPS

The JC model can be realized in ion trap with the vibrational frequency ν , where the photonic mode is replaced by the phononic mode [S8–S10]. The qubit is formed by two hyperfine ground states $|g\rangle$ and $|e\rangle$, separated by the energy ω_0 . The qubit and the phononic mode are coupled through virtual excitation of an excited state ($|f\rangle$) with a pair of laser beams with the frequencies $\omega + \omega_0 + \Delta_0 - \nu$ and $\omega + \Delta_0$, where ω is the energy difference between $|e\rangle$ and $|f\rangle$. When the detuning Δ_0 is much larger than ν and the amplitude of the laser beams, E_0 , the two laser beams couple the two ground states $|g\rangle$ and $|e\rangle$ in a Raman manner, with the strength $\chi_0 = E_0^2/\Delta_0$. Consider the system dynamics in the sideband-resolved regime $\chi_0 \ll \nu$ and in the Lamb-Dicke limit $\eta_0 = \delta k_0/\sqrt{2\nu M} \ll 1$, where δk_0 denotes the wavevector difference between the laser fields and M is the mass of the ion. Then the coupling between the internal and external degrees of freedom is described by the JC Hamiltonian

$$H_{JC} = \Omega(a^\dagger |g\rangle \langle e| + a |e\rangle \langle g|), \quad (\text{S23})$$

where $\Omega = \eta_0 \chi_0$, and a^\dagger and a denote creation and annihilation operators for the phononic mode. The phononic mode can be driven by two pairs of laser beams with the frequencies $(\omega + \omega_0 + \Delta_1 - \nu, \omega + \omega_0 + \Delta_1)$ and $(\omega + \Delta_1 - \nu, \omega + \Delta_1)$. With suitable choice of the polarizations, the two pairs of laser beams solely drive the transitions $|g\rangle \leftrightarrow |f\rangle$ and $|e\rangle \leftrightarrow |f\rangle$, respectively. When the detuning Δ_1 is much larger than ν and the amplitude of the laser beams, E_1 , these two pairs of laser beams couple $|g\rangle$ and $|e\rangle$ to the phononic mode, respectively. In the sideband-resolved regime $\chi_1 = E_1^2/\Delta_1 \ll \nu$ and in the Lamb-Dicke limit $\eta_1 = \delta k_1/\sqrt{2\nu M} \ll 1$, the resulting interactions are described by the Hamiltonian

$$H_d = \lambda(|g\rangle \langle g| + |e\rangle \langle e|)(a^\dagger + a), \quad (\text{S24})$$

where $\lambda = \eta_1 \chi_1$. We here have assumed that the two pair of laser beams have the same wavevector difference δk_1 . Since the identity operator $I = |g\rangle \langle g| + |e\rangle \langle e|$ can be discarded, the combination of H_{JC} and H_d is equivalent to the driven JC Hamiltonian.

Under the condition $\delta k_0 \gg \delta k_1$, we have $\eta_0 \gg \eta_1$ and $d\lambda/d\chi_1 \ll d\Omega/d\chi_0$. This implies that λ is much more insensitive to the fluctuation of χ_1 than Ω to the fluctuation of χ_0 . Therefore, we can set λ to be a known fixed value and use this model to estimate χ_0 . Below the critical point, the system has a unique dark state, where P_e is directly related to χ_0 by

$$P_e = \frac{1}{2} \left[1 - \sqrt{1 - (2\lambda/\eta_0 \chi_0)^2} \right]. \quad (\text{S25})$$

As the dynamics of a trapped ion can be manipulated in a well controlled manner, it is expected that the driven JCM and the associated critical metrological protocol can be readily realized in ion traps. Compared to the circuit QED architecture, the ion trap has the following advantages. Firstly, the qubit can be encoded in two hyperfine ground states of a trapped ion so that it has a long lifetime. Secondly, the electronic state of a trapped ion can be well restricted within a two-dimensional Hilbert space, so that the error due to leakage out of the qubit space is highly suppressed. Thirdly, the detection efficiency of the state of an ionic qubit can nearly reach 100% [S10], which is much higher than that achievable for superconducting qubits.

S11. SINGLE-QUBIT GATE INFIDELITIES DUE TO INACCURATE CALIBRATION OF DRIVING STRENGTHS

A single-qubit rotation around any axis on the equatorial plane of the Bloch sphere can be realized by resonantly driving the qubit with an external field. The qubit dynamics is given by the Hamiltonian

$$H_{dr} = \frac{\epsilon}{2}(e^{i\theta} |g\rangle \langle e| + e^{-i\theta} |e\rangle \langle g|), \quad (\text{S26})$$

where ϵ is the amplitude of the driving field and θ is the phase. After a time t , this Hamiltonian produces a rotation around the axis (\mathbf{n}) that has an angle θ to the x axis on the equatorial plane of the Bloch sphere, given by

$$R_{\mathbf{n}}(\phi) = \exp(-i\phi\sigma_{\mathbf{n}}/2), \quad (\text{S27})$$

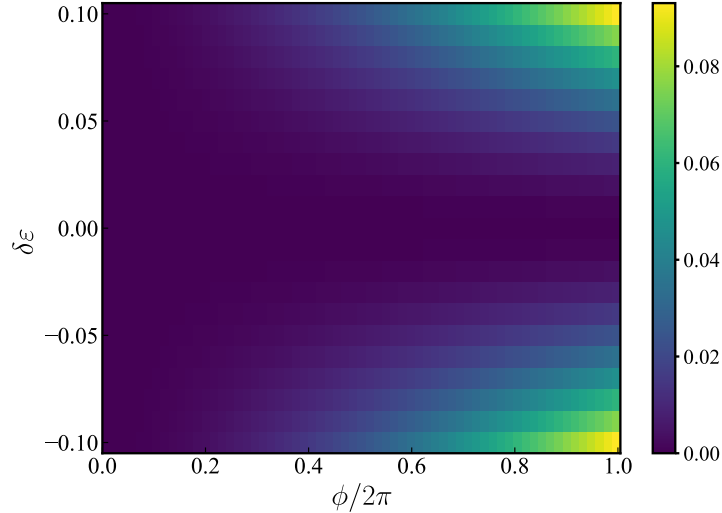


FIG. S15. Single-qubit gate infidelities versus the rotation angle ϕ and the relative deviation of the amplitude $\delta\epsilon$ of the driving field.

where $\phi = et$ and $\sigma_{\mathbf{n}} = \cos\theta\sigma_x + \sin\theta\sigma_y$, with $\sigma_x = |g\rangle\langle e| + |e\rangle\langle g|$ and $\sigma_y = i(|g\rangle\langle e| - |e\rangle\langle g|)$. A deviation of the driving amplitude from the desired value ϵ , given by $\epsilon\delta\epsilon$ would result in an error of the rotation angle, $\delta\phi = \phi\delta\epsilon$. The resulting gate error can be quantified by $1 - \mathcal{F}_p$, where \mathcal{F}_p denotes the process fidelity, defined by $\text{tr}(\chi_I\chi_\delta)$, with χ being the quantum process tomography matrix of single-qubit gate [S11]. Fig. S15 shows $1 - \mathcal{F}_p$ versus ϕ and $\delta\epsilon$. The result implies that implementation of a high-fidelity single-qubit gate requires high-precision calibration of the amplitude of the driving field. Such gates are crucial for realization of quantum algorithms [S12], as well as for multi-qubit entangled state tomography [S13]. Our protocol may be used to improve the calibration precision of the amplitudes of the driving fields used for implementation of these gates on different quantum computing platforms, including superconducting circuits and ion traps.

-
- [S1] L. Garbe, M. Bina, A. Keller, M. G. A. Paris, and S. Felicetti, Critical quantum metrology with a finite-component quantum phase transition, *Phys. Rev. Lett.* **124**, 120504 (2020).
- [S2] C. Song, S.-B. Zheng, P. Zhang, K. Xu, L. Zhang, Q. Guo, W. Liu, D. Xu, H. Deng, K. Huang, D. Zheng, X. Zhu, and H. Wang, Continuous-variable geometric phase and its manipulation for quantum computation in a superconducting circuit, *Nat. Commun.* **8**, 1061 (2017).
- [S3] W. Ning, X.-J. Huang, P.-R. Han, H. Li, H. Deng, Z.-B. Yang, Z.-R. Zhong, Y. Xia, K. Xu, D. Zheng, and S.-B. Zheng, Deterministic entanglement swapping in a superconducting circuit, *Phys. Rev. Lett.* **123**, 060502 (2019).
- [S4] R.-H. Zheng, W. Ning, Y.-H. Chen, J.-H. Lü, L.-T. Shen, K. Xu, Y.-R. Zhang, D. Xu, H. Li, Y. Xia, F. Wu, Z.-B. Yang, A. Miranowicz, N. Lambert, D. Zheng, H. Fan, F. Nori, and S.-B. Zheng, Observation of a superradiant phase transition with emergent cat states, *Phys. Rev. Lett.* **131**, 113601 (2023).
- [S5] K. Xu, Z.-H. Sun, W. Liu, Y.-R. Zhang, H. Li, H. Dong, W. Ren, P. Zhang, F. Nori, D. Zheng, H. Fan, and H. Wang, Probing dynamical phase transitions with a superconducting quantum simulator, *Sci. Adv.* **6**, eaba4935 (2020).
- [S6] M. Hofheinz, H. Wang, M. Ansmann, R. C. Bialczak, E. Lucero, M. Neeley, A. D. O'Connell, D. Sank, J. Wenner, J. M. Martinis, and A. N. Cleland, Synthesizing arbitrary quantum states in a superconducting resonator, *Nature* **459**, 546 (2009).
- [S7] C. L. Degen, F. Reinhard, and P. Cappellaro, Quantum sensing, *Rev. Mod. Phys.* **89**, 035002 (2017).
- [S8] C. Monroe, D. M. Meekhof, B. E. King, W. M. Itano, and D. J. Wineland, Demonstration of a fundamental quantum logic gate, *Phys. Rev. Lett.* **75**, 4714 (1995).
- [S9] D. M. Meekhof, C. Monroe, B. E. King, W. M. Itano, and D. J. Wineland, Generation of nonclassical motional states of a trapped atom, *Phys. Rev. Lett.* **76**, 1796 (1996).
- [S10] D. J. Wineland, Nobel lecture: Superposition, entanglement, and raising schrödinger's cat, *Rev. Mod. Phys.* **85**, 1103 (2013).
- [S11] M. Mohseni, A. T. Rezakhani, and D. A. Lidar, Quantum-process tomography: Resource analysis of different strategies, *Phys. Rev. A* **77**, 032322 (2008).
- [S12] M. A. Nielsen and I. L. Chuang, *Quantum Computation and Quantum Information: 10th Anniversary Edition*, 10th ed. (Cambridge University Press, 2011).
- [S13] C. Song, K. Xu, W. Liu, C.-p. Yang, S.-B. Zheng, H. Deng, Q. Xie, K. Huang, Q. Guo, L. Zhang, P. Zhang, D. Xu, D. Zheng, X. Zhu, H. Wang, Y.-A. Chen, C.-Y. Lu, S. Han, and J.-W. Pan, 10-qubit entanglement and parallel logic

operations with a superconducting circuit, *Phys. Rev. Lett.* **119**, 180511 (2017).